

# Interplay between Cation and Charge Ordering in $\text{La}_{1/3}\text{Sr}_{2/3}\text{FeO}_3$ Superlattices

Alex L. Krick, Chan-Woo Lee, Rebecca J. Sichel-Tissot, Andrew M. Rappe, and Steven J. May\*

The electronic properties of digital superlattices are reported, which are cation-ordered analogs of the perovskite  $\text{La}_{1/3}\text{Sr}_{2/3}\text{FeO}_3$ , a material that undergoes a charge-ordering transition. Superlattices of  $\text{LaFeO}_3$  (LFO), an antiferromagnetic insulator, and  $\text{SrFeO}_3$  (SFO), a conductor with a helical magnetic ground state, are fabricated via oxide molecular beam epitaxy. Three isocompositional superlattices with repeat structures of SSLSSL (S2), SSSL (S3), and SSSLL (S4) (S = SFO, L = LFO) are studied with cation orderings along the [001] and [111] directions for experimental and computational work, respectively. The experimental superlattice structures are confirmed via synchrotron X-ray diffraction and corresponding simulations of (00L) crystal truncation rods. The S2 and S3 superlattices are found to undergo an electronic phase transition as measured by a discontinuity in the temperature-dependent resistivity similar to the random alloy, indicating that the superlattices do not behave as a simple combination of LFO and SFO. The charge-ordering transition is not observed in the S4 sample. The electronic structure calculations using density functional theory, confirming the energetic favorability of charge ordering in the S2 and S3 structures compared to the S4 structure, are consistent with experimental trends.

## 1. Introduction

The ability to synthesize complex oxide heterostructures with single unit cell precision has enabled new scientific directions focused on understanding physical properties at oxide interfaces.<sup>[1]</sup> The formation of short-period superlattices, in which the distances between adjacent interfaces can be systematically tuned, provides an especially useful means to study how interfacial phenomena, such as charge transfer,<sup>[2–4]</sup> structural coupling,<sup>[5–8]</sup> and orbital reconstructions,<sup>[9,10]</sup> can alter or lead to new functional properties. Previous work on manganite

superlattices, in particular the  $(\text{LaMnO}_3)_m/(\text{SrMnO}_3)_n$  system, has yielded important insights into the relationships between charge transfer, electronic structure, cation disorder, and magnetic ordering.<sup>[11–15]</sup> Ferroelectric superlattices have also received considerable attention,<sup>[16–18]</sup> with short-period superlattices emerging as a platform in which to realize improper ferroelectrics.<sup>[19,20]</sup> In contrast, superlattice analogs of materials that undergo first-order electronic phase transitions, such as charge ordering, remain largely unexplored.

The iron-based perovskite  $\text{La}_{1/3}\text{Sr}_{2/3}\text{FeO}_3$  (LSFO) is an intriguing material system in which to explore the relationship between cation ordering and charge ordering. Bulk LSFO exhibits an abrupt increase in resistivity at  $T^* \approx 195$  K, due to the onset of a nominal charge-ordered state with an ordering wavevector of  $q = [1/3 \ 1/3 \ 1/3]$ .<sup>[21–23]</sup> Previous experimental and theoretical work has provided evidence that the charge ordering occurs on both Fe

and O sites due to the hybridization of Fe 3d and O 2p bands in  $\text{La}_{1-x}\text{Sr}_x\text{FeO}_3$ .<sup>[24–26]</sup> Concurrent with the charge-ordering transition is the onset of antiferromagnetism, in which a relatively long-period  $\uparrow\uparrow\downarrow\downarrow$  spin structure is stabilized along the [111] direction.<sup>[27]</sup> The spin configuration has been shown to play a key role in stabilizing the charge-ordered state.<sup>[28]</sup> While these transitions have been studied in both bulk and thin film materials,<sup>[29–34]</sup> cation-ordered equivalents of LSFO have yet to be reported, even though the 1:2 La:Sr cation ratio lends itself to short period superlattices, such as  $(\text{LaFeO}_3 (\text{LFO}))_n/(\text{SrFeO}_3 (\text{SFO}))_{2n}$ .

Using a combined experimental and computational approach, we have investigated the electronic properties of cation-ordered analogs of LSFO. We have synthesized short-period superlattices via oxide molecular beam epitaxy (MBE) in which the arrangement of LFO and SFO layers is systematically varied. While LFO and SFO films exhibit insulating and metallic behavior, respectively, the superlattices display a charge-ordering transition as indicated by a discontinuity in the temperature-dependent resistivity, the magnitude of which decreases as the interfacial density is reduced. Density functional theory (DFT) calculations provide a model to interpret the charge-ordering transition, and the layer-resolved oxygen

A. L. Krick, Dr. R. J. Sichel-Tissot, Prof. S. J. May  
Department of Materials Science and Engineering  
Drexel University  
Philadelphia, PA 19104, USA  
E-mail: smay@coe.drexel.edu

Dr. C.-W. Lee, Prof. A. M. Rappe  
The Makineni Theoretical Laboratories  
Department of Chemistry  
University of Pennsylvania  
Philadelphia, PA 19104-6323, USA



DOI: 10.1002/aelm.201500372

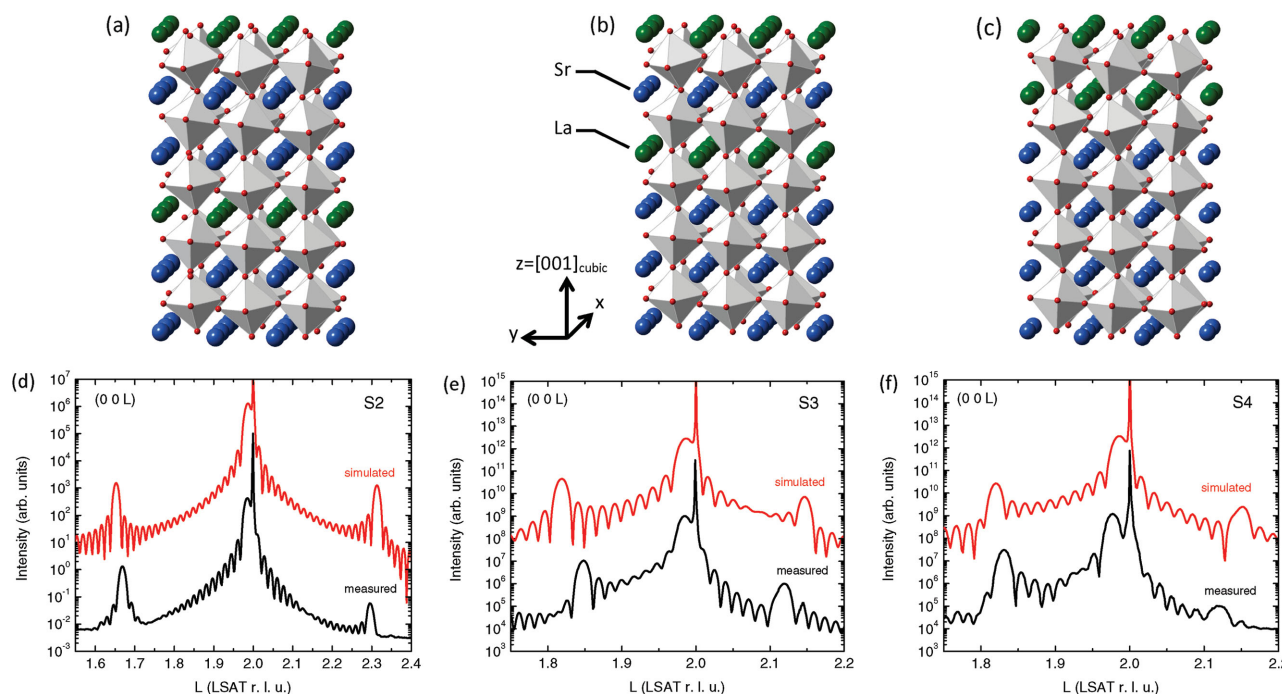


**Figure 1.** Schematics and structure of the (001)-oriented superlattices. The a) S2 a), b) S3 b), and c) S4 superlattices are layered structures in which each  $(001)_{\text{cubic}}$  plane contains identical A-site cations. The  $\text{FeO}_6$  polyhedra are shown as gray rendered solids, with oxygen atoms as red spheres at each polyhedral corner. d) Synchrotron diffraction data and simulations of the S2, S3, and S4 superlattices.

and iron oxidation states as well as local atomic structures (Fe—O—Fe bond angle) are determined from DFT calculations.

## 2. Results and Discussion

### 2.1. Structural Characterization

LSFO films and  $(\text{SFO})_n/(\text{LFO})_m$  superlattices were deposited on single crystal (001)  $(\text{LaAlO}_3)_{0.3}(\text{Sr}_2\text{AlTaO}_6)_{0.7}$  (LSAT) substrates using ozone-assisted ( $\approx 5\%$   $\text{O}_3$  in  $\text{O}_2$ ) MBE. The LSFO films were deposited by coevaporating all sources together, whereas the superlattices were deposited with alternating layers of SFO and LFO. Using this approach, we investigated three isocompositional superlattices: SSSL (S2), SSSLSL (S3), and SSSSLL (S4), where L is LFO and S is SFO, which are shown schematically in Figure 1a–c. These structures were each repeated ten times to attain a total thickness of 60 unit cells, which was fixed for both the superlattices and random alloy film.

The presence of cation ordering and layer thicknesses of the superlattices were characterized using synchrotron diffraction. Figure 1d shows the diffracted intensities of the superlattice films measured along the  $(00L)$  crystal truncation rods. The  $(002)$  peak of all the superlattices is visible at slightly lower momentum transfer than the LSAT  $(002)$  peak, consistent with the average compressive strain induced by the substrate. The average  $c$ -axis parameters of the superlattices are measured to be 3.897, 3.895, and 3.914 Å for the S2, S3, and S4 samples, respectively. Satellite peaks arising from the superlattice periodicity are clearly visible for all three samples. The presence of these satellite peaks indicates the existence of distinct LFO

and SFO unit cells. Diffraction data were simulated using the GenX package<sup>[35]</sup> to provide a comparison between the ideal targeted structures and the measured experimental data. All GenX models were simulated as idealized superlattice structures with no intermixing between the LFO and SFO layers. We used simulated  $c$ -axis parameters of 3.86 and 3.97 Å for the SFO and LFO layers, respectively, for all models.

To compare the structural accuracy of the superlattices to the targeted periodicity, we analyzed the peak positions of the first satellite peak to the left ( $-1$ ) and right ( $+1$ ) of the film  $(002)$  peak and compared the measured positions to those produced by the simulations. For the S2, we find good agreement between the measured and simulated data exhibiting a superlattice periodicity of 3.14 u.c., close to the targeted 3 u.c. The S3 and S4 samples exhibit periodicities that are 1.22 and 0.83 u.c. thicker than the targeted 6 u.c. The additional thickness from fractional unit cell layering can, in principle, be more accurately modeled in GenX with the introduction of intermixing layers. For the sake of simplicity, however, we present simulations from the idealized structures in Figure 1d. Despite the moderate error seen in the S3 and S4 periodicities, the general pattern of the cation ordering is still maintained within the S2, S3, and S4 superlattices, making the cation arrangements significantly different. In particular, the interfacial density and number of non-interfacial SFO layers is systematically increased from S2 to S4.

### 2.2. Electronic Transport

The temperature-dependent resistivity for all isocompositional samples is shown in Figure 2. The resistivity for a 60 u.c. SFO

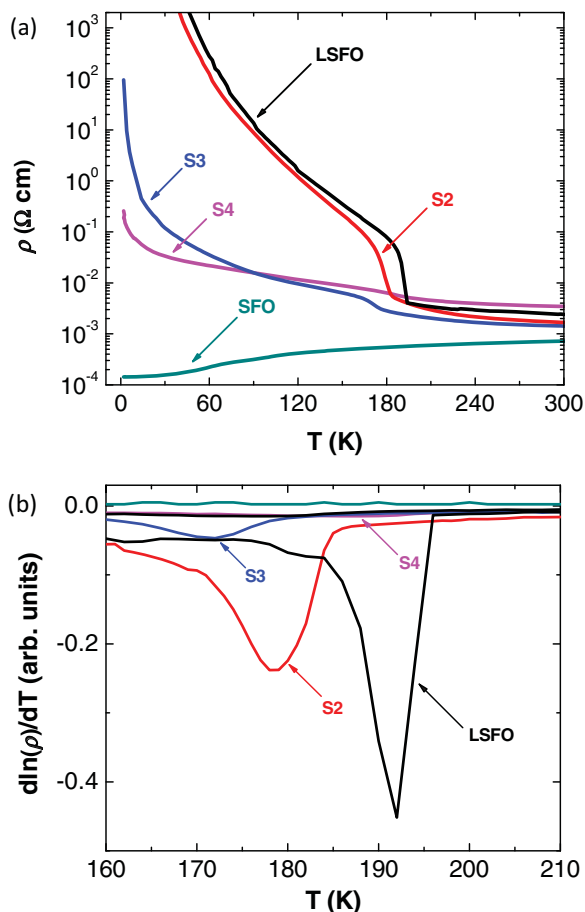


**Figure 2.** a) Temperature dependence of the resistivity for LSFO, S2, S3, S4, and SFO samples. b) The change in resistivity as a function of temperature reveals the relative sharpness and temperature of the transition. The charge-ordering transition is suppressed in the S4 sample.

film is also shown for reference and exhibits bulk-like metallic character with resistivity values that are in agreement with bulk SFO.<sup>[36]</sup> Given the stability of oxygen deficient, insulating  $\text{SrFeO}_{3-\delta}$  phases,<sup>[37,38]</sup> the observation of metallic SFO indicates that the postgrowth annealing is effective in minimizing oxygen vacancies. Pure LFO films are highly resistive, with  $\rho > 10^4 \Omega$  cm at 300 K.<sup>[39]</sup> While the LSFO random alloy and superlattice films exhibit similar room temperature resistivity of 2–5 m $\Omega$  cm, the samples differ markedly in their temperature-dependent resistivity. Both the random alloy and S2 samples exhibit abrupt increases in resistivity, consistent with an electronic phase transition. The transition temperature ( $T^*$ ), here defined as the maximum of the second derivative of resistivity with respect to temperature ( $d^2\ln(\rho)/dT^2$ ), is 194 K for the random alloy and 183 K for the S2 superlattice. As can be seen in Figure 2b, the magnitude of the fractional resistivity change ( $d\ln(\rho)/dT$ )<sup>[40]</sup> is also larger in the alloy compared to the S2 sample. Below the transition, both the random alloy and S2 share nearly identical transport behavior, with the S2 having slightly lower resistivity. Temperature-dependent synchrotron diffraction measurements from the random alloy film at the (4/3 4/3 4/3) position are shown in Figure S1 (see the Supporting Information). The emergence of the (4/3 4/3 4/3) peak

below  $T^*$  indicates that the change in resistivity arises from a charge-ordering transition, as in bulk  $\text{La}_{1/3}\text{Sr}_{2/3}\text{FeO}_3$ .<sup>[21,22,31,41]</sup> The similarity of the resistivity data obtained from the random alloy and S2 samples suggests that the cation ordering in S2 does not alter the charge-ordering pattern, which is supported by density functional theory calculations discussed below.

The S3 superlattice shows a slight increase in resistivity near 176 K, though both the magnitude of  $d\ln(\rho)/dT$  and  $T^*$  ( $=176$  K) are reduced compared to the S2. The transition is apparently suppressed in the S4 sample, suggesting that the charges are no longer ordered. At low temperatures, all superlattices exhibit insulating behavior; the resistivity systematically depends on the number of consecutive SFO layers, with  $\rho_{S4} < \rho_{S3} < \rho_{S2}$  below 50 K.

These results demonstrate that the charge ordering is dependent on the cation ordering and the number of consecutive  $\text{FeO}_6$  octahedra enclosed between SrO layers within each superlattice period. In particular, the resistivity data indicate that as the cation ordering is changed from S2 to S4, the propensity for charge ordering is suppressed, a result that is consistent with first-principles calculations described below. The suppression of charge ordering is most apparent in the S4 sample where three consecutive  $\text{FeO}_6$  octahedra enclosed between SrO layers are stacked in a repeating manner through the superlattice. The electronic transport of the S4 sample exhibits weakly insulating temperature dependence until roughly 5 K, below which a large upturn in resistivity is displayed. We attribute the insulating behavior, as opposed to metallic behavior observed in the SFO film, to the finite thickness of the SFO layers, as previous studies of other metallic perovskites such as  $\text{LaNiO}_3$  have revealed metal–insulator transitions upon reducing film thickness below 4–7 u.c.<sup>[42–45]</sup> By contrast, transport in the S2 closely resembles the random alloy, suggesting that the electronic concentration is relatively uniform across the superlattice in spite of the cation ordering. The transport similarities in the S2 and random alloy are consistent with behavior observed in  $(\text{LaMnO}_3)_2/(\text{SrMnO}_3)_1$  superlattices, which exhibit slightly reduced resistivity compared to  $\text{La}_{2/3}\text{Sr}_{1/3}\text{MnO}_3$  alloy films but with a minimal effect on magnetic-ordering temperature.<sup>[46,47]</sup> In these short-period manganite systems, both DFT calculations and Monte Carlo simulations confirmed the homogeneity of the charge density through the superlattice.<sup>[48,49]</sup> Finally, we note that magnetization measurements were carried out on the superlattices using a vibrating sample magnetometer; no evidence of ferromagnetic ordering was observed in the superlattices (see Figure S2 in the Supporting Information). We were unable to measure a cusp in the magnetic susceptibility at the Néel temperature in our films and superlattices, which we attribute to the limited sample volume. We note that previous work on  $\text{La}_{1/3}\text{Sr}_{2/3}\text{FeO}_3$  has shown that the charge and antiferromagnetic (AFM) orderings occur at the same temperature,<sup>[28,31]</sup> and thus we anticipate that the measured  $T^*$  also marks the Néel temperature of the samples.

### 2.3. Correlation between A-Site Cation Ordering and Spin Ordering

DFT calculations were performed to better understand the relationships between cation ordering, the spin configuration,

and charge ordering. Three different isocompositional LSFO models corresponding to S2, S3, and S4 were constructed based on a rhombohedral 30-atom LSFO cell ( $R\bar{3}c$  space group). In the models, the ordering directions of A-site cations and spin configurations of Fe ions are both [111]; defined based on a pseudocubic cell. Each (111) plane has a uniform layer of A-site cations (either Sr or La) and spin configurations. For each LSFO model system, 32 different spin configurations for Fe ions have been compared (six Fe ion planes with either up or down spins for each ion, using global up-down symmetry). Since a charge and spin density wave has been observed experimentally along [111] in LSFO, we believe that this assumption of [111] spin planes is reasonable.<sup>[22,27]</sup> At this point, it should be mentioned that the ordering direction of A-site cations for the LSFO models, [111], is different from experimental ordering direction, [001]. Experimentally, synthesizing short-period (111)-oriented superlattices presents a more significant technical challenge compared to (001)-oriented superlattices, in which nominal unit cell control can be readily realized. However, considering that the major role of A-site cation ordering in LSFO is expected to be variations of the oxidation states of Fe and O, we believe that comparison of the experimental and theoretically obtained trends provide qualitative insight into the contribution of A-site cation ordering to the spin configuration of LSFO.

We first describe how Sr ordering in LSFO changes the stable spin configuration, which is believed to play a central role in stabilizing the charge ordering.<sup>[28]</sup> Figure 3 compares four important spin configurations (a, b, c, and d) with the energy difference ( $\Delta E$ ) compared to the most stable spin structure for the three cation-ordered structures.  $\Delta E$  between the four stable configurations, and others not shown here, is on the order of 0.1 eV cell<sup>-1</sup>. AFM arrangements a and b describe the bulk spin ordering of LSFO. Configuration c is commonly referred to as G-type antiferromagnetism, in which each Fe spin is antiparallel with its six nearest Fe neighbors, thus maximizing AFM interactions.

For both S3 and S4, the most stable spin configuration is a. However, it is unclear for S2 which configuration is the most stable one. Specifically, even though configuration c has the

lowest total energy, its energy difference from bulk spin ordering of LSFO (configurations a and b) is miniscule (<0.01 eV LSFO<sup>-1</sup>). This value is smaller than the error range associated with our convergence threshold for  $k$ -points and cutoff energy. Thus, we believe that it is reasonable to expect that configurations a and b are comparably stable with configuration c.

All of the lowest energy spin structures lead to insulating behavior. However, the magnitude of the energy gap decreases as the Sr cations become increasingly clustered (S2  $\rightarrow$  S4); the calculated band gaps are 0.3 eV (S2), 0.3 eV (S3), and 0.1 eV (S4). This trend is consistent with the trend in resistivity experimentally observed, even though the crystallographic direction of cation ordering differs.

Our calculations also show that cation ordering alters the relative stability of the nonground state spin structures. Particularly, nonideal spin configuration d becomes increasingly stable as the number of consecutive SFO layers increases from S2 to S4. For S2 and S3, energy of configuration d is rather high with reference to the most stable spin structure ( $\Delta E = 0.07$ – $0.1$  eV cell<sup>-1</sup>). By contrast,  $\Delta E$  in S4 is 0.007 eV cell<sup>-1</sup>, which is smaller than that of S2 and S3 by an order of magnitude. Interestingly, S4 with the d spin configuration is metallic.

To examine how Sr ordering acts on charge ordering, layer-resolved charges of Fe and O of spin configuration  $\uparrow\downarrow\downarrow\uparrow\uparrow$  for all LSFO models are estimated using Bader charge analysis, as shown in Figure 4.<sup>[50,51]</sup> As seen in Figure 3, S3 and S4 show the lowest DFT energies with this  $\uparrow\downarrow\downarrow\uparrow\uparrow$  configuration. In S2, due to infinitesimal DFT energy difference among three configurations including the  $\uparrow\downarrow\downarrow\uparrow\uparrow$ , it is not clear which one is the most favorable configuration.

In Bader analysis, charge density is partitioned as distinct regions for adjacent ions by defining boundaries satisfying the condition of  $\nabla\rho(r) = 0$  where  $\rho(r)$  is the electron charge density. Thus, charge from Bader analysis is not constrained to be an integer like other theoretical approaches based on electronic structure calculations.<sup>[51]</sup> While direct quantitative comparison among oxidation state and local charge of ions can be challenging,<sup>[52]</sup> the qualitative trend of oxidation states can be favorably captured by Bader charges as reported by other studies.<sup>[53,54]</sup>

First, all models show Fe<sup>1.90+</sup>–Fe<sup>1.88+</sup>–Fe<sup>1.88+</sup>–Fe<sup>1.90+</sup>–Fe<sup>1.88+</sup>–Fe<sup>1.88+</sup> charge ordering with some minor deviation dependent on Sr distribution which is consistent with bulk LSFO (peaks at Fe1 and Fe4). This “high–low–low–high–low–low” pattern along the [111] direction is identical with the experimentally proposed charge ordering (Fe<sup>5+</sup>–Fe<sup>3+</sup>–Fe<sup>3+</sup>–Fe<sup>5+</sup>–Fe<sup>3+</sup>–Fe<sup>3+</sup>) which is based on an ionic bonding picture.<sup>[28]</sup> Appreciable modulation of the hole density on the oxygen ions, as shown in Figure 4c, is also consistent with previous unrestricted Hartree–Fock calculations.<sup>[24]</sup> For O, the charge magnitude is minimized at O1, O3, O4, and O6, which are the adjacent O layers to Fe1 and Fe4. This difference in Bader charges ( $\approx 0.02$  for Fe and  $\approx 0.08$  for O) is on the same order of magnitude with Bader charges of other materials.<sup>[53,54]</sup>

The Bader charge trend in Figure 4b illustrates how the Sr distribution affects both charge and spin orderings. Bader charges of Fe in S2, where the Sr distribution is closer to bulk LSFO than to S3 and S4, show a symmetric spatial profile. As Sr clusters (S2  $\rightarrow$  S4), the Fe charge pattern becomes

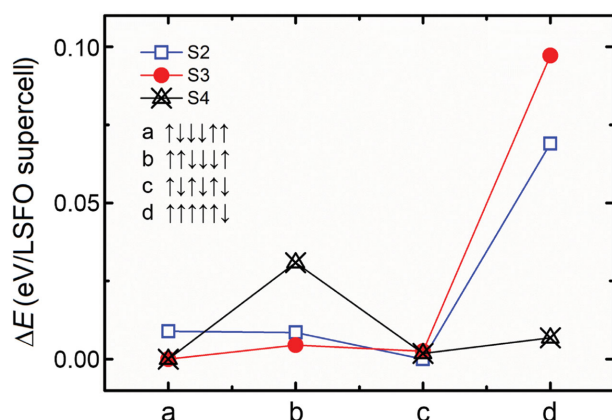


**Figure 3.** Energy calculated by DFT +  $U$  for four different spin configurations for each LSFO cation configuration.  $\Delta E$  is the energy difference of the LSFO model with each spin configuration with respect to that of the most stable configuration.

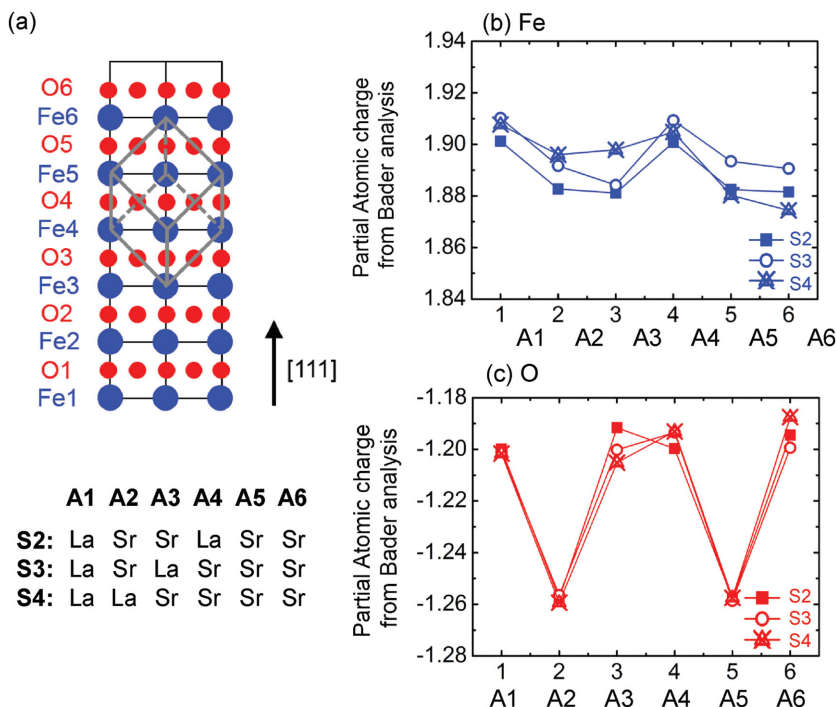


**Figure 4.** a) Schematic description showing cation ordering along [111] direction. The Fe and O charges from Bader analysis for spin structure  $\uparrow\downarrow\downarrow\uparrow\uparrow$  of all three LSFO models are shown in (b) and (c), respectively.

asymmetric, with contributions from the A-site charge superimposed on the charge-ordering pattern. In S3, the Bader charge is concentrated in two regions (A1–A2 and A4–A6) with a drop in charge at A3. In the A1–A2 layers, holes are more concentrated in S4 with respect to S2. This region of increased charge density in S4 occurs in the La-rich portion of the superlattice. This observation illustrates how the electron source of S3 is different from that of S4. Carriers in S3 are derived from aliovalent substitution effect ( $\text{Sr}'_{\text{La}}$  using Kröger–Vink notation) as Sr and La cations in S3 act in a manner analogous to LSFO bulk. However, the layers of higher Bader charge in S4 originate from the LFO-like region. Specifically, as Sr is completely clustered in S4, the superlattice increasingly behaves as separate LFO-like and SFO-like regions. Thus, Fe Bader charges become higher in the La rich region (A1–A2) than in the Sr rich region (A3–A6) because Bader charge of Fe in bulk LFO ( $\text{Fe}^{1.86+}$ ) is higher than that of bulk SFO ( $\text{Fe}^{1.64+}$ ). This Bader charge difference of Fe among LFO and SFO is opposite to the trend from an ionic picture ( $\text{Fe}^{3+}$  in LFO and  $\text{Fe}^{4+}$  in SFO) in which explicit electron transfer from Fe to O is assumed. One potential interpretation for the opposite behavior is that SFO has increased covalent bonding among Fe and O due to its negative charge transfer energy ( $\Delta \approx -3.0$  eV) in comparison with that of LFO ( $\Delta \approx +4.0$  eV). Thus, back electron transfer from Fe to O can be predominant in SFO in contrast to LFO.<sup>[55]</sup> Calculated Bader charge of O in SFO ( $\text{O}^{1.07-}$ ) in this study is significantly higher than that in LFO ( $\text{O}^{1.32-}$ ). While an additional investigation of Fe oxidation states in LFO and SFO is beyond the scope of our study since we intend to determine reference Bader charges to examine charge-ordering behavior

of LSFO, future research could tackle this issue in-depth.

Our interpretations of the electronic distribution within the S4 superlattice offer an insight into the correlation among cation ordering and ground state spin structure shown in Figure 3. Specifically, the reason that the energetic stability of configuration d becomes similar to configurations a and c in S4 is because the La-rich and Sr-rich regions become increasingly like bulk LFO or SFO compared to the S2 or S3.

In addition to the charge distribution throughout the superlattices, the DFT results also reveal the presence of spatially varying Fe–O–Fe bond angles ( $\theta$ ) arising from *aaa*-type rotations of the  $\text{FeO}_6$  octahedra. A smaller variation in  $\theta$  is present in the S2 superlattice than the S4 superlattice. In the S2, the calculated bond angles range from  $160.1^\circ$  to  $164.1^\circ$ . In the S4 superlattice,  $\theta$  values between  $158.0^\circ$  and  $165.5^\circ$  are obtained, with the highest bond angles in the Sr-rich regions and the lowest bond angles in the La-rich regions. This trend is similar to the electronic distribution, with the S2 superlattice exhibiting more homogeneous atomic structure compared to the S4 superlattice.

The increased variation in  $\theta$  may also play a role in destabilizing the charge ordering, as previous work on bulk  $\text{RSr}_{2/3}\text{FeO}_3$ , where R is a rare earth cation, has shown that the charge-ordering transition is not present in compounds with a reduced tolerance factor ( $R = \text{Sm}$  and  $\text{Gd}$ ).<sup>[23]</sup>

### 3. Conclusions

In summary, we have systematically studied the effect of cation ordering on the electronic phase transition in  $(\text{LaFeO}_3)_n/(\text{SrFeO}_3)_m$  superlattices that are compositionally equivalent to  $\text{La}_{1/3}\text{Sr}_{2/3}\text{FeO}_3$ . Our results show that the formation of superlattices with systematic changes to the cation arrangements generates macroscopic electronic behavior that cannot be treated as simple combinations of the constituent materials. The charge-ordered state is suppressed in the S4 compared to the S2, as demonstrated by electronic transport measurements and DFT calculations. DFT calculations reveal that charge ordering and corresponding stable spin configuration is suppressed as Sr cations are clustered, illustrating that the individual  $\text{LaFeO}_3$  and  $\text{SrFeO}_3$  layers exhibit increasingly bulk-like behavior as the distance between interfaces is increased. These results elucidate the relationship between cation ordering, which acts to alter local electronic configurations, and electronic phase transitions, in which nonuniform electronic configurations emerge from macroscopically homogeneous oxidation states. This work provides a direct demonstration of how atomically controlled synthesis of oxide heterostructures can be used to tailor the stability of charge-ordered states.

## 4. Experimental Section

**Experimental Techniques:** LSFO films and  $(\text{SFO})_n/(\text{LFO})_m$  superlattices were deposited using an oxide MBE system from Omicron/Scienta (modified LAB-10). Metal cations were sublimated or evaporated using Knudsen cells containing elemental La, Sr, and Fe. The surface crystalline quality was monitored in situ using reflection high-energy electron diffraction. During the growth, the temperature was  $625 \pm 25$  °C at an ozone pressure of  $2 \times 10^{-6}$  Torr. To improve the nominal oxygen stoichiometry, all samples were annealed postgrowth in a tube furnace (Thermo Scientific Lindberg Blue M) at atmospheric pressure under flowing  $\text{O}_2$  at 675 °C for 3 h, immediately followed by an additional anneal under flowing  $\text{O}_2/\text{O}_3$  ( $\approx 95\%/5\%$ ) at 200 °C for 30 min. This two-step annealing process is an effective method to reduce oxygen vacancies. Synchrotron X-ray diffraction measurements were completed at Sector 33-BM-C of the Advanced Photon Source using a photon energy of 10.0 keV. Electrical resistivity measurements were obtained in a Physical Properties Measurement System (PPMS) (Quantum Design EverCool II) using an external Keithley 6220 current source and Keithley 2148 Nanovoltmeter. A linear four-point probe measurement geometry was used for all measurements. Magnetometry measurements were performed in the PPMS using the vibrating sample magnetometry option.

**Density Functional Theory Calculations:** We performed DFT calculations using the Quantum ESPRESSO package,<sup>[56]</sup> employing the generalized gradient approximation<sup>[57]</sup> with pseudopotentials constructed by the Rappe–Rabe–Kaxiras–Joannopoulos scheme<sup>[58]</sup> and the designed nonlocal method.<sup>[59]</sup> Pseudopotentials for La, Sr, Fe, and O atoms were developed using the open-source pseudopotential generator, OPIUM<sup>[60]</sup> with  $5s^2 5p^6 6s^0 4f^0 5d^0 6p^0$ ,  $4s^2 4p^6 5s^0 4d^1$ ,  $3s^2 3p^6 4s^2 3d^5 1 4p^0$ , and  $2s^2 2p^4$  as their reference configurations, respectively. Nonlinear core corrections were included with the Fe and Sr pseudopotentials to obtain better descriptions of the electronic structures of LSFO.<sup>[61]</sup> In addition, a Hubbard  $U$  of 4.4 eV was applied to Fe in order to describe energy gaps of LSFO accurately. The  $U$  value was determined from self-consistent linear-response calculations of LFO bulk.<sup>[62]</sup> Also,  $k$ -point meshes ( $3 \times 3 \times 3$ ) and cutoff energy (55 Ry) were chosen to achieve a convergence error of 0.01 eV  $\text{LSFO}^{-1}$  ( $\approx 0.2$  meV  $\text{atom}^{-1}$ ) in the total energy. The ions in each atomic structure were fully relaxed toward equilibrium until the forces were less than 0.001 Ry  $a_0^{-1}$ .

## Supporting Information

Supporting Information is available from the Wiley Online Library or from the author.

## Acknowledgements

A.L.K. and C.-W.L. contributed equally to this work. A.L.K., R.J.S.-T., C.-W.L., and S.J.M. were supported by the U.S. Office of Naval Research under Grant No. N00014-11-1-0664. A.M.R. was supported by the U.S. Department of Energy under Grant No. DE-FG02-07ER46431. C.-W.L. also acknowledges partial support from Korea Institute of Energy Research (KIER) under the framework of Research and Development Program (B5-2514). Acquisition of the PPMS was supported by the Army Research Office under Grant W911NF-11-1-0283. Use of the Advanced Photon Source, an Office of Science User Facility operated for the U.S. Department of Energy (DOE) Office of Science by Argonne National Laboratory, was supported by the U.S. DOE under Contract No. DE-AC02-06CH11357. The authors acknowledge computational support from the National Energy Research Scientific Computing center program.

Received: October 28, 2015

Revised: February 26, 2016

Published online: April 5, 2016

- [1] H. Y. Hwang, Y. Iwasa, M. Kawasaki, B. Keimer, N. Nagaosa, Y. Tokura, *Nat. Mater.* **2012**, *11*, 103.
- [2] C. W. Lin, S. Okamoto, A. J. Millis, *Phys. Rev. B* **2006**, *73*, 041104.
- [3] A. Ohtomo, D. A. Muller, J. L. Grazul, H. Y. Hwang, *Nature* **2002**, *419*, 378.
- [4] S. Yunoki, A. Moreo, E. Dagotto, S. Okamoto, S. S. Kancharla, A. Fujimori, *Phys. Rev. B* **2007**, *76*, 064532.
- [5] A. Y. Borisevich, H. J. Chang, M. Huijben, M. P. Oxley, S. Okamoto, M. K. Niranjan, J. D. Burton, E. Y. Tsymlal, Y. H. Chu, P. Yu, R. Ramesh, S. V. Kalinin, S. J. Pennycook, *Phys. Rev. Lett.* **2010**, *105*, 087204.
- [6] J. Hwang, J. Son, J. Y. Zhang, A. Janotti, C. G. Van de Walle, S. Stemmer, *Phys. Rev. B* **2013**, *87*, 060101.
- [7] C. L. Jia, S. B. Mi, M. Faley, U. Poppe, J. Schubert, K. Urban, *Phys. Rev. B* **2009**, *79*, 081405.
- [8] J. M. Rondinelli, S. J. May, J. W. Freeland, *MRS Bull.* **2012**, *37*, 261.
- [9] J. Chakhalian, J. W. Freeland, H. U. Habermeier, G. Cristiani, G. Khaliullin, M. van Veenendaal, B. Keimer, *Science* **2007**, *318*, 1114.
- [10] P. Yu, J. S. Lee, S. Okamoto, M. D. Rossell, M. Huijben, C. H. Yang, Q. He, J. X. Zhang, S. Y. Yang, M. J. Lee, Q. M. Ramasse, R. Erni, Y. H. Chu, D. A. Arena, C. C. Kao, L. W. Martin, R. Ramesh, *Phys. Rev. Lett.* **2010**, *105*, 027201.
- [11] S. J. May, P. J. Ryan, J. L. Robertson, J. W. Kim, T. S. Santos, E. Karapetrova, J. L. Zarestky, X. Zhai, S. G. E. te Velthuis, J. N. Eckstein, S. D. Bader, A. Bhattacharya, *Nat. Mater.* **2009**, *8*, 892.
- [12] E. J. Monkman, C. Adamo, J. A. Mundy, D. E. Shai, J. W. Harter, D. W. Shen, B. Burganov, D. A. Muller, D. G. Schlom, K. M. Shen, *Nat. Mater.* **2012**, *11*, 855.
- [13] P. A. Salvador, A. M. Haghiri-Gosnet, B. Mercey, M. Hervieu, B. Raveau, *Appl. Phys. Lett.* **1999**, *75*, 2638.
- [14] T. S. Santos, B. J. Kirby, S. Kumar, S. J. May, J. A. Borchers, B. B. Maranville, J. Zarestky, S. G. E. T. Velthuis, J. van den Brink, A. Bhattacharya, *Phys. Rev. Lett.* **2011**, *107*, 167202.
- [15] J. Verbeeck, O. I. Lebedev, G. Van Tendeloo, B. Mercey, *Phys. Rev. B* **2002**, *66*, 184426.
- [16] H. N. Lee, H. M. Christen, M. F. Chisholm, C. M. Rouleau, D. H. Lowndes, *Nature* **2005**, *433*, 395.
- [17] N. Sai, B. Meyer, D. Vanderbilt, *Phys. Rev. Lett.* **2000**, *84*, 5636.
- [18] M. P. Warusawithana, E. V. Colla, J. N. Eckstein, M. B. Weissman, *Phys. Rev. Lett.* **2003**, *90*, 036802.
- [19] E. Bousquet, M. Dawber, N. Stucki, C. Lichtensteiger, P. Hermet, S. Gariglio, J. M. Triscone, P. Ghosez, *Nature* **2008**, *452*, 732.
- [20] J. M. Rondinelli, C. J. Fennie, *Adv. Mater.* **2012**, *24*, 1961.
- [21] J. Herrero-Martin, G. Subias, J. Garcia, J. Blasco, M. C. Sanchez, *Phys. Rev. B* **2009**, *79*, 045121.
- [22] J. Q. Li, Y. Matsui, S. K. Park, Y. Tokura, *Phys. Rev. Lett.* **1997**, *79*, 297.
- [23] S. K. Park, T. Ishikawa, Y. Tokura, J. Q. Li, Y. Matsui, *Phys. Rev. B* **1999**, *60*, 10788.
- [24] J. Matsuno, T. Mizokawa, A. Fujimori, Y. Takeda, S. Kawasaki, M. Takano, *Phys. Rev. B* **2002**, *66*, 193103.
- [25] T. Saha-Dasgupta, Z. S. Popovic, S. Satpathy, *Phys. Rev. B* **2005**, *72*, 045143.
- [26] H. Wadati, A. Chikamatsu, R. Hashimoto, M. Takizawa, H. Kumigashira, A. Fujimori, M. Oshima, M. Lippmaa, M. Kawasaki, H. Koinuma, *J. Phys. Soc. Jpn.* **2006**, *75*, 054704.
- [27] P. D. Battle, T. C. Gibb, P. Lightfoot, M. Matsuo, *J. Solid State Chem.* **1990**, *85*, 38.
- [28] R. J. McQueeney, J. Ma, S. Chang, J. Q. Yan, M. Hehlen, F. Trouw, *Phys. Rev. Lett.* **2007**, *98*, 126402.
- [29] J. Blasco, B. Aznar, J. Garcia, G. Subias, J. Herrero-Martin, J. Stankiewicz, *Phys. Rev. B* **2008**, *77*, 054107.

- [30] R. C. Devlin, A. L. Krick, R. J. Sichel-Tissot, Y. J. Xie, S. J. May, *J. Appl. Phys.* **2014**, *115*, 233704.
- [31] J. Okamoto, D. J. Huang, K. S. Chao, S. W. Huang, C. H. Hsu, A. Fujimori, A. Masuno, T. Terashima, M. Takano, C. T. Chen, *Phys. Rev. B* **2010**, *82*, 132402.
- [32] W. Prellier, B. Mercey, *J. Phys. D: Appl. Phys.* **2002**, *35*, L48.
- [33] K. Ueno, A. Ohtomo, F. Sato, M. Kawasaki, *Phys. Rev. B* **2006**, *73*, 165103.
- [34] H. Wadati, D. Kobayashi, H. Kumigashira, K. Okazaki, T. Mizokawa, A. Fujimori, K. Horiba, M. Oshima, N. Hamada, M. Lippmaa, M. Kawasaki, H. Koinuma, *Phys. Rev. B* **2005**, *71*, 035108.
- [35] M. Björck, G. Andersson, *J. Appl. Crystallogr.* **2007**, *40*, 1174.
- [36] S. Ishiwata, M. Tokunaga, Y. Kaneko, D. Okuyama, Y. Tokunaga, S. Wakimoto, K. Kakurai, T. Arima, Y. Taguchi, Y. Tokura, *Phys. Rev. B* **2011**, *84*, 054427.
- [37] P. Adler, A. Lebon, V. Damljanovic, C. Ulrich, C. Bernhard, A. V. Boris, A. Maljuk, C. T. Lin, B. Keimer, *Phys. Rev. B* **2006**, *73*, 094451.
- [38] J. P. Hodges, S. Short, J. D. Jorgensen, X. Xiong, B. Dabrowski, S. M. Mini, C. W. Kimball, *J. Solid State Chem.* **2000**, *151*, 190.
- [39] Y. J. Xie, M. D. Scafetta, E. J. Moon, A. L. Krick, R. J. Sichel-Tissot, S. J. May, *Appl. Phys. Lett.* **2014**, *105*, 062110.
- [40] R. Schmidt, *Phys. Rev. B* **2008**, *77*, 205101.
- [41] R. J. Sichel-Tissot, R. C. Devlin, P. J. Ryan, J.-W. Kim, S. J. May, *Appl. Phys. Lett.* **2013**, *103*, 212905.
- [42] G. Gou, I. Grinberg, A. M. Rappe, J. M. Rondinelli, *Phys. Rev. B* **2011**, *84*, 144101.
- [43] S. J. May, T. S. Santos, A. Bhattacharya, *Phys. Rev. B* **2009**, *79*, 115127.
- [44] R. Scherwitzl, S. Gariglio, M. Gabay, P. Zubko, M. Gibert, J. M. Triscone, *Phys. Rev. Lett.* **2011**, *106*, 246403.
- [45] J. Son, P. Moetakef, J. M. LeBeau, D. Ouellette, L. Balents, S. J. Allen, S. Stemmer, *Appl. Phys. Lett.* **2010**, *96*, 062114.
- [46] C. Adamo, X. Ke, P. Schiffer, A. Soukiassian, M. Warusawithana, L. Maritato, D. G. Schlom, *Appl. Phys. Lett.* **2008**, *92*, 112508.
- [47] A. Bhattacharya, S. J. May, S. G. E. te Velthuis, M. Warusawithana, X. Zhai, B. Jiang, J. M. Zuo, M. R. Fitzsimmons, S. D. Bader, J. N. Eckstein, *Phys. Rev. Lett.* **2008**, *100*, 257203.
- [48] S. Dong, R. Yu, S. Yunoki, G. Alvarez, J. M. Liu, E. Dagotto, *Phys. Rev. B* **2008**, *78*, 064414.
- [49] B. R. K. Nanda, S. Satpathy, *Phys. Rev. B* **2009**, *79*, 054428.
- [50] R. F. W. Bader, *Atoms in Molecules: A Quantum Theory*, Oxford University Press, Oxford, **1994**.
- [51] G. Henkelman, A. Arnaldsson, H. Jónsson, *Comput. Mater. Sci.* **2006**, *36*, 354.
- [52] H. Raebiger, S. Lany, A. Zunger, *Nature* **2008**, *453*, 763.
- [53] K. G. Reeves, Y. Kanai, *J. Chem. Phys.* **2014**, *141*, 024305.
- [54] M. Xu, P. Xiao, S. Stauffer, J. Song, G. Henkelman, J. B. Goodenough, *Chem. Mater.* **2014**, *26*, 3089.
- [55] S. F. Matar, P. Mohn, G. Demazeau, *J. Magn. Magn. Mater.* **1995**, *140–144*, 169.
- [56] G. Paolo, B. Stefano, B. Nicola, C. Matteo, C. Roberto, C. Carlo, C. Davide, L. C. Guido, C. Matteo, D. Ismaila, C. A. Dal, G. Stefano de, F. Stefano, F. Guido, G. Ralph, G. Uwe, G. Christos, K. Anton, L. Michele, M.-S. Layla, M. Nicola, M. Francesco, M. Riccardo, P. Stefano, P. Alfredo, P. Lorenzo, S. Carlo, S. Sandro, S. Gabriele, P. S. Ari, S. Alexander, U. Paolo, M. W. Renata, *J. Phys.: Condens. Matter* **2009**, *21*, 395502.
- [57] J. P. Perdew, K. Burke, M. Ernzerhof, *Phys. Rev. Lett.* **1996**, *77*, 3865.
- [58] A. M. Rappe, K. M. Rabe, E. Kaxiras, J. D. Joannopoulos, *Phys. Rev. B* **1990**, *41*, 1227.
- [59] N. J. Ramer, A. M. Rappe, *Phys. Rev. B* **1999**, *59*, 12471.
- [60] E. J. Walter, <http://opium.sourceforge.net>, **2015**.
- [61] S. G. Louie, S. Froyen, M. L. Cohen, *Phys. Rev. B* **1982**, *26*, 1738.
- [62] M. Cococcioni, S. de Gironcoli, *Phys. Rev. B* **2005**, *71*, 035105.